A multi phase-field-cohesive zone model for laminated composites: Application to delamination migration

P.K. Asur Vijaya Kumar [a,b], A. Dean [c,b,*], J. Reinoso [b], M. Paggi [a]

[a] IMT School for Advanced Studies Lucca, Piazza San Francesco 19, 55100 Lucca, Italy
[b] Elasticity and Strength of Materials Group, School of Engineering, Universidad de Sevilla, Camino de los Descubrimientos s/n, 41092 Seville, Spain
[c] School of Civil Engineering, Sudan University of Science and Technology, PO Box 72 Eastern Daim, Khartoum, Sudan

ABSTRACT

Failure processes in Laminated Fiber-Reinforced Composites (LFRCs) entail the development and progression of different physical mechanisms and, in particular, the interaction between inter-laminar and intra-laminar cracking. Reliable modeling of such complex scenarios can be achieved by developing robust numerical predictive tools that allow for the interaction of both failure modes. In this study, a novel Multi Phase-Field (MPF) model relying on the Puck theory of failure for intra-laminar failure at ply level is coupled with a Cohesive Zone Model (CZM) for inter-laminar cracking. The current computational method is numerically implemented as a system of non-linear coupled equations using the finite element method via user-defined `UMAT` and `UEL` subroutines in `ABAQUS`. The computational tool is applied to qualitatively predict delamination migration in long laminated fiber-reinforced polymers composites comprising 44 cross-ply laminates. The reliability of the current approach is examined via the correlation with experimental results. Finally, the present study is complemented with additional representative examples with the aim of providing further insight into the potential role of different aspects of the system in the delamination migration, including (i) the variation of the ply angle in the migration zone, (ii) the load application point, and (iii) initial crack length.

1. Introduction

The widespread use of Laminated Fiber Reinforced Composites (LFRCs) due to their high strength to weight ratios has paved their way into many practical applications in different industrial sectors, with remarkable impact in aerospace and aeronautics, and more recently in the automotive sector [1,2], to quote a few of them. In the presence of ever-increasing demands of new technological advancements, load-bearing capabilities and failure modes of these materials are not yet fully understood, posing notable restrictions on their use and leading to the introduction of high safety factors.

Within this context, delamination failure can be conceived as one of the most critical failure mechanisms in Laminated Fiber Reinforced Composites (LFRCs). Such cracking events are generally associated with low through-thickness stiffness in layered disposals and can emerge from manufacturing defects, the occurrence of post-buckling phenomena [3,4], among many others. From a modeling standpoint, delamination events in layered composites structures have been analyzed using linear elastic fracture mechanics (LEFM), enforcing

initiation and growth along the ply interface with the use of strain energy-based methods in order to define the corresponding fracture toughness [5,6]. Delamination can be found in low-velocity impact [7], skin debonding [8], defects from notches [9,10], among many other practical cases. These phenomena have been extensively investigated based on cohesive-like cracking methods in pre-notched coupon configurations. An ad-hoc inter-laminar failure model can be inserted into the most critical locations of the specimen for triggering such cracking events [11–14]. From a mechanical perspective, delamination can be seen as a result of the coalescence of micro-cracks at the ply interface, perpendicular to the tensile stress [15–17].

However, for some specific loading cases and configurations, it has been reported that mostly due to the change of the sign of shearing stresses, a pre-existing crack along the ply interface can kink out from such location, propagating into the adjacent ply. Matrix-cracking induced by delamination can further progress through the ply thickness and then "propagates out" at another interface as reported in [15,18,19], leading to the so-called "delamination migration" failure mode. Thus, following the terminologies used in [20], the turning of

* Corresponding author at: School of Civil Engineering, Sudan University of Science and Technology, PO Box 72 Eastern Daim, Khartoum, Sudan.
E-mail addresses: pavan.asur@imtlucca.it (P.K. Asur Vijaya Kumar), a.dean@sustech.edu (A. Dean).

delamination crack front into one of the adjacent plies is referred to as "kinking," whereas, when a crack propagates across the thickness of plies and propagates out in adjacent interface is called "migration" [21]. The main causes of such phenomena can be motivated by the analysis of the stress field around the interface crack tip, see the experimental studies conducted in [15,22,19] for a $0°/90°$ interface and [16] for a $0°/\theta°$ interface.

In the last decade, the advent of new numerical capabilities and modeling techniques has promoted the thorough analysis of the potential reasons for the driving mechanisms that provoke delamination migration failures [23]. Note also that the migration phenomenon is also observed in the models without the presence of pre-existing cracks [22]. Numerical methods such a eXtended FEM (XFEM) [24], augmented finite element methods [25], floating node methods [26], cohesive-crack element methods [27] have been widely applied to study delamination migration. Moreover, delamination migration can be explained using micro-mechanics as reported by Arteiro and coauthors [28].

Concerning the different modeling methods for triggering intralaminar failure in LFRCs, the use of continuum damage mechanics (CDM)-based methods have been of notable importance; see the phenomenological models proposed in [29,30,44] and the references given therein. Notwithstanding, the local versions of CDM models generally suffer from mesh pathological issues that can be remedied using alternative methodologies. Nonlocal damage models [31,32] have been used extensively, which also share as part of phase-field formalism while providing a detailed description of the damage behavior. On the other hand, theories such as crack band theory have been extensively used in the literature to mitigate spurious mesh sensitivity in the modeling location. In this direction, substantial contributions from Bažant are noteworthy, see [33–37] and the reference therein. Within this framework, Phase-field (PF) methods, originally proposed by Francfort and Marigo [38] and subsequently developed in [39], have become plausible nonlocal modeling alternatives that prevent most of the main limitations of alternative modeling tools for fracture in solids. With strong foundations on Griffith's approach to Fracture Mechanics, PF methods exploit a multi-field variational formalism, whereby fracture is accounted for via diffusive representation within a particular region of the domain characterized by the length-scale l. The Phase-field method for fracture integrates classical damage mechanics and Griffith's theory of failure. This generalized formalism can handle topologically complex fractures such as initiation, branching of the crack, intersection of crack, coalescence of damage, etc., or combining them in two and three-dimensional settings without any ad hoc. This approach encompasses an energy minimization of the potential energy of the body (split into bulk and fracture counterparts, respectively), resulting in a multi-field FE formulation. Therefore, complex cracking phenomena can be naturally captured due to the implicit consideration of the corresponding crack phase-field variables' evolution equation. Posterior developments of PF techniques for fracture have been oriented towards the analysis of alternative formulations [40,41], shells [30], ductile fracture [42–44], composite materials [45–51], heterogeneous media [48], hydrogen assisted cracking [52], among many others, and from a numerical point of view striving for different solution strategies [53]. The authors have recently proposed incorporating phenomenological failure criteria for composite materials widening the range of applicability of PF methods for different composite materials [54].

In this investigation, the two phase-field fracture model proposed by the authors in [55] is combined with a cohesive zone model following a bi-linear traction separation law in order to predict the development of such failure events in LFRCs. Consequently, at the intra-ply level, the driving force for each of the failure mechanisms within the PF technique, i.e., fiber failure and inter-fiber failure, is exploited independently. Moreover, this fracture model is readily applied to capture the kinking and migration events along with delamination. The pro-

posed model is examined against experimental data available in the related literature for validating the predictive capabilities of the current simulation technique. In addition to the previous aspects, the present study also encompasses the analysis of the variation of design parameters for which physical solution favors delamination-migration, such as load application point, angle of the ply at the interfaces, and initial crack length. Such effects are studied to understand each of the variation's load-bearing capacity and show the applicability of the proposed model to predict complex failure phenomena.

The manuscript is organized as follows. In Section 2, the Multi Phase-Field-Cohesive Zone (MPF-CZ) formulation based on the Puck failure theory is introduced. In Section 3, the variational formulation of the proposed model, along with the strong form, is outlined with a special focus on the construction of the contribution for each failure mechanism. In Section 4, the finite element implementation of the model is derived. The assessment of the proposed framework for its validation is discussed in Section 5 in conjunction with a further investigation concerning the variation of the systems with respect to several design parameters. Finally, Section 6 summarizes the main conclusions of the present study.

2. Multi Phase-Field-Cohesive Zone (MPF-CZ) formulation based on the Puck failure theory

In this section, the computational framework herein proposed for capturing delamination migration in layered composite structures is outlined. The current method relies on the combination of multiple phase-fields. Each phase-field based on different physically motivated failure mechanisms such as Puck failure criterion [55] driving the crack propagation in long fiber reinforced polymer composites along with the cohesive zone model.

Following the standard Phase-field formulation, let to consider an arbitrary body in the general n_{dim} Euclidean space, occupying the placement $\mathscr{B} \in \mathbb{R}^{n}_{dim}$, with its external delimiting boundary $\partial \mathscr{B} \in \mathbb{R}^{n_{dim}-1}$, see Fig. 1. For any material point, the position vector is denoted by $\mathbf{x} \in \mathscr{B}$. The displacement field is identified by the vector $\mathbf{u} : \mathscr{B} \to \mathbb{R}^{n}_{dim}$, with infinitesimal stain tensor $\boldsymbol{\varepsilon} := \nabla^s \mathbf{u}$ for $\boldsymbol{\varepsilon} : \mathscr{B} \to \mathbb{R}^{n_{dim} \times n_{dim}}$. The displacement boundary conditions are prescribed as $\mathbf{u} = \overline{\mathbf{u}}$ on $\partial \mathscr{B}_u$ and traction conditions are given by $\overline{\mathbf{t}} = \boldsymbol{\sigma} \cdot \mathbf{n}$ on $\partial \mathscr{B}_t$ such that, kinematic and static boundary conditions satisfy: $\overline{\partial \mathscr{B}_t \cup \partial \mathscr{B}_u} = \partial \mathscr{B}$ and $\partial \mathscr{B}_t \cap \partial \mathscr{B}_u = \varnothing$, where $\mathbf{n}$ is outward normal vector and $\boldsymbol{\sigma}$ is the Cauchy stress tensor.

In addition to the previous definitions, let Γ be a crack set incorporating interface cracks Γ_i arising from the cohesive interface and cracks in the bulk $\Gamma_{\mathfrak{d}_t}$ from the multi phase-field such that, $\Gamma_i \cup \Gamma_{\mathfrak{d}_t} = \Gamma$ and $\Gamma_i \cap \Gamma_{\mathfrak{d}_t} = \varnothing$ for each discrete $t \in [0, T]$ with $\Gamma_t \subseteq \Gamma_{t+1}$. The displacement jumps along the interface as the relative displacement between two homogeneous points at the flanks are denoted by $\mathfrak{g} = \mathbf{u}_i^+ - \mathbf{u}_i^-$, representing the difference between kinematic field along the interface Γ_i^+ and Γ_i^- in line with [56,57]. On the other hand, $\Gamma_{\mathfrak{d}_t}$ is defined as the set of discontinuous points $\mathbf{x}$, where $\mathbf{u}$ has one sided approximate limits $\mathbf{u}_{\mathfrak{d}}^+ \neq \mathbf{u}_{\mathfrak{d}}^-$ with respect to a suitable direction υ_u normal to $\Gamma_{\mathfrak{d}_t}$ inline with [58,59].

In order to account for multiple energies in the system, the total free energy functional describing the mechanics of body $\mathscr{B}$, is given as the sum total of internal and external energies acting on the body as follows:

$$\Pi(\mathbf{u}, \Gamma) = \Pi_{int}(\mathbf{u}, \Gamma) + \Pi_{ext}(\mathbf{u}). \tag{1}$$

Phase-field approximation of the fracture relies on the idea that the fracture propagates due to competition between elastic energy stemming from the state function of strain tensor $\boldsymbol{\varepsilon}$ and fracture energy (surface energy) stemming from scalar internal damage like variable $\mathfrak{d}$[55]. The consistent generalization of the isotropic damage formulation for the consideration of different failure mechanisms can be
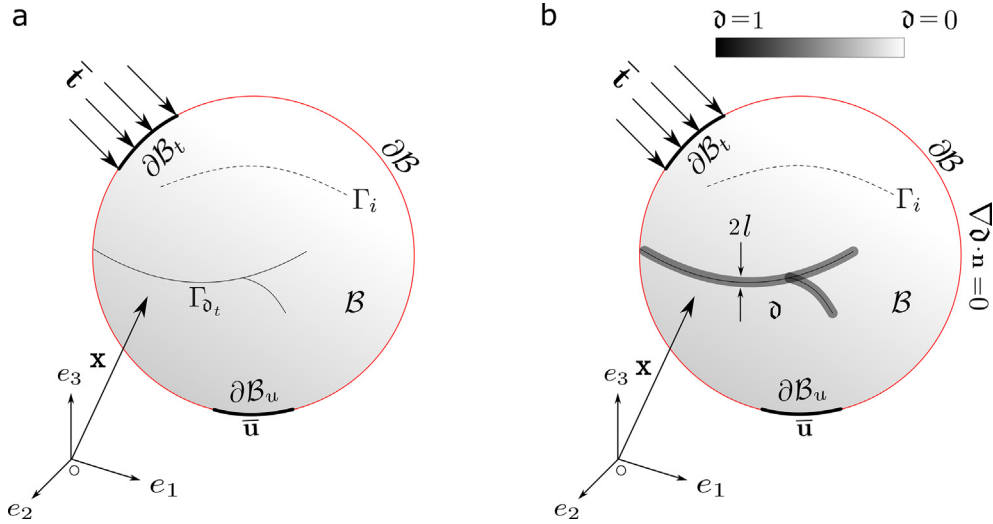
Fig. 1. Body under consideration: (a) sharp crack representation and (b) Regularized crack topology.

postulated by the additive decomposition of total internal energy into multiple contributions, in which each of them is associated with a certain failure mechanism. In such a postulation, a scalar damage variable $\mathfrak{d}_i$ $(i = 1, \ldots, n)$ is associated with each one of the n failure mechanisms, such that $\mathfrak{d}_i = 0$ for intact material state and $\mathfrak{d}_i = 1$ for fully broken state and so that $\mathfrak{d}_i \in [0, 1]$ for each $i = 1, \ldots, n$. Moreover, in order to account for non-local damage evolution, the respective gradients $\nabla_{\mathbf{x}} \mathfrak{d}_i$ are incorporated in the formulation. This additive decomposition for intralaminar failure was successfully applied in [29] and later extended to incorporate failure criteria such as Puck failure theory so as to distinguish between the fiber and matrix dominated damage mechanisms in LFRPs [55,30]. However, the consideration of dissipative energies stemming from debonding along the interface Γ_i, and crack propagation in the bulk $\Gamma_{\mathfrak{d}_t}$ is still a matter of investigation. The prediction of such crack topology becomes increasingly complex due to branching and coalescence phenomenons, as well as the interaction with diffusive cracks, which may induce the debonding process along the existing interface Γ_i. One possibility to achieve this is by employing a phase-field model incorporating multiple diffusive crack fields within the bulk and interface elements relying on cohesive zone methodologies at a prescribed interface inline with [57]. Hence, the total internal energy is now an amalgamation of (i) total elastic energy constituting from bulk (fiber and inter-fiber) energy, (ii) surface energy (crack energy) stemming from bulk (fiber and inter-fiber) failure, and (iii) cohesive interface energy obeying a bi-linear traction-separation law:

$$\Pi_{\text{int}}(\mathbf{u}, \Gamma) = \Pi_{\text{int},b}(\mathbf{u}, \Gamma_{\mathfrak{d}_i}) + \Pi_{\text{int},c}(\Gamma_i), \tag{2}$$

where $\Pi_{int,b}(\mathbf{u}, \Gamma)$ is the internal energy stemming from the bulk (fiber and inter-fiber) and $\Pi_{int,c}(\Gamma_i)$ is the dissipative energy associated with cohesive debonding which are addressed in detail in the sequel. The bulk energy $\Pi_{int,b}(\mathbf{u}, \Gamma)$ is further decomposed into:

$$\Pi_{\text{int},b}(\mathbf{u}, \Gamma_{\mathfrak{d}_i}) = \Pi_{\text{int},FF}(\mathbf{u}, \Gamma_{\mathfrak{d}_{FF}}) + \Pi_{\text{int},IFF}(\mathbf{u}, \Gamma_{\mathfrak{d}_{IFF}}), \tag{3}$$

where $\Pi_{int,FF}(\mathbf{u}, \Gamma_{\mathfrak{d}_{FF}})$ and $\Pi_{int,IFF}(\mathbf{u}, \Gamma_{\mathfrak{d}_{IFF}})$ correspond to the energies associated with fiber failure and inter-fiber failure, respectively.

With such decomposition at hand, the scheme herein used recalls that the dissipated energy arising from each of the individual failure mechanisms only affects their corresponding counterparts in the elasticity tensor. This, therefore precludes the coupling between fiber, inter-fiber failures and each of these failures with respect to the cohesive debonding. Note that, due to this preclusion of interaction

between the energies, the elastic energy is strongly coupled with the surface energies stemming from fiber, inter-fiber, and cohesive debonding. In contrast, surface energies among themselves are only weakly coupled.

The effective Helmholtz free energy function $\hat{\Psi}$ is defined as:

$$\hat{\Psi}(\boldsymbol{\varepsilon}, \mathbf{A}) = \frac{1}{2} \boldsymbol{\varepsilon} : \mathbb{C}^e : \boldsymbol{\varepsilon}, \tag{4}$$

where $\mathbb{C}^e$ is the undamaged elastic constitutive tensor defined as:

$$\mathbb{C}^e := \partial_{\varepsilon\varepsilon} \hat{\Psi}$$
$$= \lambda \mathbf{1} \otimes \mathbf{1} + 2\mu_T \mathbb{I} + \alpha(\mathbf{1} \otimes \mathbf{A} + \mathbf{A} \otimes \mathbf{1}) + 2(\mu_L - \mu_T)\mathbb{I}_A + \beta \mathbf{A} \otimes \mathbf{A}, \tag{5}$$

where $\mathbf{1}$ is the second order identity tensor, $\mathbb{I}_{A,ijkl} = A_{im}\mathbb{I}_{jmkl} + A_{jm}\mathbb{I}_{mikl}$ represents the fourth-order identity matrix, and $\lambda, \alpha, \beta, \mu_T$ and μ_L are to the elastic constants taking the form:

$$\lambda = E_{22}(\nu_{23} + \nu_{31}\nu_{13})/D, \tag{6}$$

$$\alpha = E_{22}[\nu_{31}(1 + \nu_{32} - \nu_{13}) - \nu_{32}]/D, \tag{7}$$

$$\beta = E_{11}(1 - \nu_{32}\nu_{23})/D - E_{22}[1 - \nu_{21}(\nu_{12} + 2(1 + \nu_{23}))]/D - 4G_{12}, \tag{8}$$

$$\mu_L = G_{12}; \mu_T = G_{23}, \tag{9}$$

with $D = 1 - \nu_{32}^2 - 2\nu_{13}\nu_{31} - 2\nu_{32}\nu_{13}\nu_{31}$. The material direction is denoted by $\mathbf{a}$ and $\mathbf{A} := \mathbf{a} \otimes \mathbf{a}$ is so called structural tensor.

Here, 1-direction corresponds to the fiber orientation, 2-direction is transverse in-plane orientation with respect to the fiber direction, and 3-direction stands for transverse out-of-plane orientation.

2.1. Bulk energies

In the light of previous developments, the total energy of the fiber can be established as the sum total of the elastic energy and fracture energy associated with the fiber:

$$\Pi_{\text{int},FF}(\mathbf{u}, \Gamma_{\mathfrak{d}_{FF}}) \approx \Pi_{\text{int},FF}(\mathbf{u}, \mathfrak{d}_{FF}) = \int_{\mathscr{B}} (1 - \mathfrak{d}_{FF})^2 \hat{\Psi}_{FF}(\boldsymbol{\varepsilon}, \mathbf{A}) d\Omega$$
$$+ \int_{\mathscr{B}} \mathscr{G}_{c,FF} \left[\frac{1}{2l_{FF}} \mathfrak{d}_{FF}^2 + \frac{l_{FF}}{2} |\nabla \mathfrak{d}_{FF}|^2 \right] d\Omega, \tag{10}$$

where $\hat{\Psi}_{FF}$ is the elastic contribution associated with the fiber: $\hat{\Psi}_{FF} = \frac{1}{2} \boldsymbol{\varepsilon} : \mathbb{C}^e_{FF} : \boldsymbol{\varepsilon}$, where:

$$
\mathbb{C}_{FF}^e = \begin{bmatrix} \mathbb{C}_{11}^e & 0 & 0 & 0 & 0 & 0 \\ 0 & 0 & 0 & 0 & 0 & 0 \\ 0 & 0 & 0 & 0 & 0 & 0 \\ 0 & 0 & 0 & 0 & 0 & 0 \\ 0 & 0 & 0 & 0 & 0 & 0 \\ 0 & 0 & 0 & 0 & 0 & 0 \end{bmatrix}, \tag{11}
$$

and $\mathscr{G}_{c,FF}$ is the fracture energy, and l_{FF} is the material characteristic length associated with fiber failure in phase-field related to the apparent material strength [60] as:

$$
l_{FF} = \frac{27}{256} \frac{E_{11} \mathscr{G}_{c,FF}}{\sigma_{s,FF}^2}, \tag{12}
$$

where $\sigma_{s,FF}$ is the apparent material strength associated with fiber failure.

Similarly, the inter-fiber contribution to the total internal energy can be expressed as:

$$
\Pi_{\text{int},IFF}(\mathbf{u}, \Gamma_{\mathfrak{d}_{FF}}) \approx \Pi_{\text{int},IFF}(\mathbf{u}, \mathfrak{d}_{IFF}) = \int_{\mathscr{B}} (1 - \mathfrak{d}_{IFF})^2 \hat{\Psi}_{IFF}(\boldsymbol{\varepsilon}, \mathbf{A}) d\Omega
$$
$$
+ \int_{\mathscr{B}} \mathscr{G}_{c,IFF} \left[\frac{1}{2 l_{IFF}} \mathfrak{d}_{IFF}^2 + \frac{l_{IFF}}{2} |\nabla \mathfrak{d}_{IFF}|^2 \right] d\Omega, \tag{13}
$$

where $\hat{\Psi}_{IFF} = \frac{1}{2} \boldsymbol{\varepsilon} : \mathbb{C}_{IFF}^e : \boldsymbol{\varepsilon}$ is the elastic contribution associated with the inter-fiber failure, and:

$$
\mathbb{C}_{IFF}^e = \begin{bmatrix} 0 & \mathbb{C}_{12}^e & \mathbb{C}_{13}^e & 0 & 0 & 0 \\ \mathbb{C}_{21}^e & \mathbb{C}_{22}^e & \mathbb{C}_{23}^e & 0 & 0 & 0 \\ \mathbb{C}_{31}^e & \mathbb{C}_{32}^e & \mathbb{C}_{33}^e & 0 & 0 & 0 \\ 0 & 0 & 0 & \mathbb{C}_{44}^e & 0 & 0 \\ 0 & 0 & 0 & 0 & \mathbb{C}_{55}^e & 0 \\ 0 & 0 & 0 & 0 & 0 & \mathbb{C}_{66}^e \end{bmatrix}. \tag{14}
$$

where $\mathscr{G}_{c,IFF}$ and l_{IFF} are the fracture energy and corresponding length scale associated with inter-fiber failure, respectively. Similarly, the length scale parameter is estimated for the apparent material strength $\sigma_{s,IFF}$ of inter-fiber failure as:

$$
l_{IFF} = \frac{27}{256} \frac{E_{22} \mathscr{G}_{c,IFF}}{\sigma_{s,IFF}^2}. \tag{15}
$$

Note that with these definitions at hand, the damaged constitutive matrix $\mathbb{C}$ renders:

$$
\mathbb{C}(\mathfrak{d}_{FF}, \mathfrak{d}_{IFF}) = (1 - \mathfrak{d}_{FF})^2 \mathbb{C}_{FF}^e + (1 - \mathfrak{d}_{IFF})^2 \mathbb{C}_{IFF}^e, \tag{16}
$$

$$
\mathbb{C}(\mathfrak{d}_{FF}, \mathfrak{d}_{IFF}) = \begin{bmatrix} \mathscr{P}_1 \mathbb{C}_{11}^e & \mathscr{P}_2 \mathbb{C}_{12}^e & \mathscr{P}_2 \mathbb{C}_{13}^e & 0 & 0 & 0 \\ \mathscr{P}_2 \mathbb{C}_{21}^e & \mathscr{P}_2 \mathbb{C}_{22}^e & \mathscr{P}_2 \mathbb{C}_{23}^e & 0 & 0 & 0 \\ \mathscr{P}_2 \mathbb{C}_{31}^e & \mathscr{P}_2 \mathbb{C}_{32}^e & \mathscr{P}_2 \mathbb{C}_{33}^e & 0 & 0 & 0 \\ 0 & 0 & 0 & \mathscr{P}_{12} \mathbb{C}_{44}^e & 0 & 0 \\ 0 & 0 & 0 & 0 & \mathscr{P}_{12} \mathbb{C}_{55}^e & 0 \\ 0 & 0 & 0 & 0 & 0 & \mathscr{P}_2 \mathbb{C}_{66}^e \end{bmatrix}, \tag{17}
$$

where $\mathscr{P}_1 = (1 - \mathfrak{d}_{FF})^2, \mathscr{P}_2 = (1 - \mathfrak{d}_{IFF})^2$, and $\mathscr{P}_{12} = \min(\mathscr{P}_1, \mathscr{P}_2)$. Notice that $\mathscr{P}_{12}$ is not differentiable due to the existence of "min". Hence, we first take the minima so that, any minimum of $\mathscr{P}_{12}$ (i.e $\mathscr{P}_1$ or $\mathscr{P}_2$) is differentiable.

2.2. Interface energies

The energy stemming from the interface is governed by a bi-linear traction separation law which constitutes of a linear elastic stage characterized by an initial stiffness of K_n, K_{t1} and K_{t2} corresponding to the normal and shear components, respectively, followed by a linear softening as in Fig. 2. The irreversibility is accounted for by the inroduc-
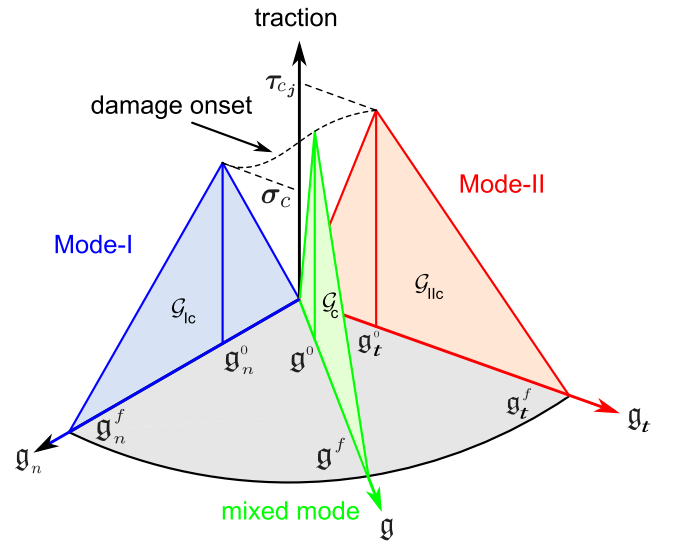

Fig. 2. Schematic representation of the bi-linear cohesive zone model traction-separation law for mixed mode.

tion of a scalar-based damage variable $\mathfrak{d}_c$ depending on the relative kinematic critical normal and tangential openings, $\mathfrak{g}_n^f$ and $\mathfrak{g}_{t_j}^f$ ($j = 1$ for 2D and $j = 1, 2$ for 3D), respectively [12,13].

The corresponding interface laws governing the normal and tangential tractions σ_n and τ_{t_j}, respectively, take the form:

$$
\boldsymbol{\sigma}_n = \begin{cases} k_n \mathfrak{g}_n & \text{if } \mathfrak{g}_n \leqslant \mathfrak{g}_n^0 \\ (1 - \mathfrak{d}_c) k_n \mathfrak{g}_n & \text{if } \mathfrak{g}_n^0 < \mathfrak{g}_n < \mathfrak{g}_n^f, \\ 0 & \text{Otherwise} \end{cases} \tag{18}
$$

$$
\boldsymbol{\tau}_{t_j} = \begin{cases} k_{t_j} \mathfrak{g}_{t_j} & \text{if } \mathfrak{g}_{t_j} \leqslant \mathfrak{g}_{t_j}^0 \\ (1 - \mathfrak{d}_c) k_{t_j} \mathfrak{g}_{t_j} & \text{if } \mathfrak{g}_{t_j}^0 < \mathfrak{g}_{t_j} < \mathfrak{g}_{t_j}^f, \\ 0 & \text{Otherwise} \end{cases} \tag{19}
$$

for each $j = 1, 2$ to account for the tangential traction, whereas $\mathfrak{g}_n$ and $\mathfrak{g}_{t_j}$ are the relative normal and tangential displacements, respectively. The Mixed-mode fracture energy of the interface reads:

$$
\mathscr{G}_C^i = \mathscr{G}_{IC} + (\mathscr{G}_{IIC} - \mathscr{G}_{IC}) \left(\frac{\mathscr{G}_{II} + \mathscr{G}_{III}}{\mathscr{G}_I + \mathscr{G}_{II} + \mathscr{G}_{III}} \right)^\eta, \tag{20}
$$

where $\mathscr{G}_{IC}, \mathscr{G}_{IIC}$, and $\mathscr{G}_{IIIC}$ represent the corresponding fracture toughness associated with normal (Mode I) and shear (Mode II and III), respectively, and computed as the area under the traction separation curve, η identifies an experimental fitting parameter elucidating the effects of fracture mode mixities [4]. Finally, $\mathscr{G}_I, \mathscr{G}_{II}$, and $\mathscr{G}_{III}$ are energy release rate associated with Mode I, Mode II, and III, respectively. Damage is initiated using the quadratic interaction function of nominal stress ratios. The damage is evolved using Benzeggagh-Kenane (BK) failure criterion based on cumulative energy such that mixed fracture toughness $\mathscr{G}_C^i$ reaches the critical energy.

Based on the energy considerations, the evolution of the damage variable $\mathfrak{d}_c$ is estimated based on the effective displacement of the cohesive element, where $\mathfrak{d}_c$ is evolving linearly with:

$$
\mathfrak{d}_c = \frac{\mathfrak{g}_m^f (\mathfrak{g}_m^{\max} - \mathfrak{g}_m^0)}{\mathfrak{g}_m^{\max} (\mathfrak{g}_m^f - \mathfrak{g}_m^0)}, \tag{21}
$$

where $\mathfrak{g}_m^0$ is effective displacement at initiation and $\mathfrak{g}_m^f = \frac{2 \mathscr{G}_C}{T_{eff}^0}$ is the effective displacement at failure. Here, T_{eff}^0 is the effective traction at damage initiation estimated using effective tractions

$T_{eff} = \sqrt{(\sigma_n)^2 + (\tau_{t_1})^2 + (\tau_{t_2})^2}$, as $T_{eff}^0 = \min\{T_{eff}(\mathfrak{d}_c > 0)\}$. And $\mathfrak{g}_m^{max}$ refers to the maximum value of effective displacement during loading history estimated using $\mathfrak{g}_m^{max} = \max_{[0,T]} \mathfrak{g}_m$, where $\mathfrak{g}_m := \sqrt{\langle \mathfrak{g}_n^2 \rangle + (\mathfrak{g}_{t_1})^2 + (\mathfrak{g}_{t_2})^2}$. Finally, with this at hand, the corresponding total energy generated by the cohesive interface takes the form:

$$\Pi_{int,c}(\Gamma_i) \approx \Pi_{int,c}(\mathfrak{d}_c) = \int_{\Gamma_i} \mathscr{G}_c^i(\mathfrak{g}, \mathfrak{d}_c) \mathrm{d}\mathscr{S} = \int_{\Gamma_i} \mathfrak{g}^T \mathscr{T} \mathrm{d}\mathscr{S}, \tag{22}$$

with $\mathfrak{g} = [\mathfrak{g}_n, \mathfrak{g}_{t_1}]$ and $\mathscr{T} = [\sigma_n, \tau_{t_1}]$.

2.3. Fundamentals of Puck failure criterion

Damage evolution within the bulk relies on Puck failure theory [61], whose corresponding failure criterion accounts for the independent assessment of fiber and inter-fiber failure surfaces. For the fiber failure, with usual notations, that is $\parallel$ (subscript 1), $\perp$ (subscript 2 and subscript 3) representing fiber direction, normal to the fiber direction in-plane and, normal to the fiber direction out-of-plane, respectively, for the ply co-ordinates in a local setting $0 - \mathbf{e}_1 - \mathbf{e}_2 - \mathbf{e}_3$ as in Fig. 3.

According to the Puck theory, fiber failure is triggered based on energetic considerations that, the exposure factor (denoted $f_{E,FF+}$, for tensile only) reaches the value 1, where $f_{E,FF+}$ is given by:

$$f_{E,FF+} = \frac{1}{R_\parallel^t}\left[\sigma_{11} - \left(\nu_{\perp\parallel} - \frac{E_\parallel}{E_{\parallel f}}\nu_{\perp\parallel f}\right)(\sigma_{22} + \sigma_{33})\mathscr{P}_2\right], \tag{23}$$

where $R_\parallel^t$ stands for the tensile longitudinal strength in fiber direction. $\nu_{\perp\parallel}$ and $\nu_{\perp\parallel f}$ identify the major Poisson's ratios of the ply and the fibers, respectively, and $E_{\parallel f}$ is the elastic modulus of the fibers. $FF+$ denotes the fiber failure in tension, whereas the compression is omitted for the sake of brevity but can easily be incorporated as in [55]. The incorporation of $\mathscr{P}_2$ is to scale the influence of the transverse stress components on the longitudinal stress (lateral contraction) with respect to the state of matrix damage. It is assumed that the contraction in the longitudinal direction due to transverse stress would vanish in a case $\mathscr{P}_2 \to 1$, i.e., matrix rupture parallel to the fibers. In the case of compressive longitudinal stress, reduced compressive longitudinal fracture resistance of the plies is assumed in the case of increasing shear stress.

Puck theory also distinguishes the inter-fiber failure by introducing the so-called action plane [62,61], which corresponds to identifying the potential fracture plane derived from the maximum stress states $\{\bar{\sigma}_n(\Theta), \bar{\tau}_{nt}(\Theta), \bar{\tau}_{n1}(\Theta)\}$, where $\bar{\sigma}_n(\Theta), \bar{\tau}_{nt}(\Theta)$, and $\bar{\tau}_{n1}(\Theta)$ are the normal stress component, shear stress component transverse to the fiber,
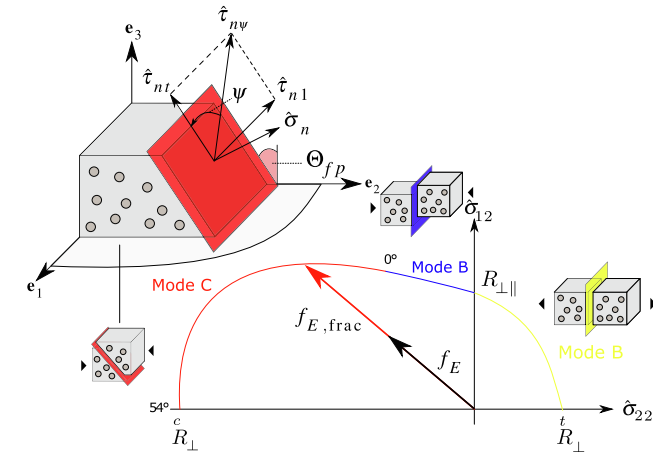
Fig. 3. Puck failure theory: (a) definition of acting stresses on the fracture plane by θ_{fp} angle and (b) the exposure factor f_E, where $f_{E,(fr)}$ is the exposure factor at the failure point.

and the shear stress component plane parallel to the fiber, respectively, each on the action plane. The determination of the fracture plane is usually performed via the assessment of the most critical stress state in terms of the local components by calculating the value of inter-fiber exposure factor $F_{E,IFF}$ for all angles Θ within the interval of $-90° \leqslant \Theta \leqslant +90°$, using an increment of one degree. The transformation from the local ply setting to the action plane system yields:

$$\begin{bmatrix} \sigma_n(\Theta) \\ \tau_{nt}(\Theta) \\ \tau_{n1}(\Theta) \end{bmatrix} = \begin{bmatrix} \cos^2\Theta & \sin^2\Theta & 2\cos\Theta\sin\Theta & 0 & 0 \\ -\cos\Theta\sin\Theta & \cos\Theta\sin\Theta & \cos^2\Theta - \sin^2\Theta & 0 & 0 \\ 0 & 0 & 0 & \sin\Theta & \cos\Theta \end{bmatrix} \begin{bmatrix} \sigma_{22} \\ \sigma_{33} \\ \sigma_{23} \\ \sigma_{13} \\ \sigma_{12} \end{bmatrix}. \tag{24}$$

In particular, the expression for inter-fiber failure under tensile conditions on the action plane takes the form:

$$f_{E,IFF+}(\Theta) = \left[\sqrt{\left[\left(\frac{1}{R_\perp^{At}} - \frac{p_{\perp\psi}^t}{R_{\perp\psi}^A}\right)\sigma_n(\Theta)\right]^2 + \left(\frac{\tau_{nt}(\Theta)}{R_{\perp\perp}^A}\right)^2 + \left(\frac{\tau_{n1}(\Theta)}{R_\parallel^A}\right)^2} + \frac{p_{\perp\psi}^t}{R_{\perp\psi}^A}\sigma_n(\Theta)\right] \frac{1}{\eta_w} \text{ for } \sigma_n(\Theta) \geqslant 0, \tag{25}$$

where $R_\perp^{At}$ and $R_{\perp\perp}^A$ are transverse tensile strength and fracture strength respectively, whereas $R_{\perp\psi}^A$ is the transverse tensile strength at any ply angle ψ, with $f_{E,IFF+}$ representing the exposure factor and the failure is triggered when $f_{E,IFF+}$ reaches the value 1.

In the previous expression, $\cos^2\psi$ and $\sin^2\psi$ are:

$$\cos^2\psi = \frac{\tau_{nt}^2}{\tau_{nt}^2 + \tau_{n1}^2} \text{ and } \sin^2\psi = \frac{\tau_{n1}^2}{\tau_{nt}^2 + \tau_{n1}^2}. \tag{26}$$

Finally, the definition of the inclination parameters $p_{\perp\psi}^t$ and $p_{\perp\psi}^c$ for any angle ψ renders:

$$\frac{p_{\perp\psi}^i}{R_{\perp\psi}^A} = \frac{p_{\perp\perp}^i}{R_{\perp\perp}^A}\cos^2\psi + \frac{p_{\perp\parallel}^i}{R_{\perp\parallel}^A}\sin^2\psi, i = t, c; \tag{27}$$

with:

$$R_{\perp\psi}^A = \left[\left(\frac{\cos\psi}{R_{\perp\perp}^A}\right)^2 + \left(\frac{\sin\psi}{R_{\perp\parallel}^A}\right)^2\right]. \tag{28}$$

Due to the modelling assumptions herein made, the proposed model requires the following fracture energy values: (i) $\mathscr{G}_{c,FF}$ fiber fracture energy, (ii) $\mathscr{G}_{c,IFF}$ matrix dominated fracture energy, and (iii) $\mathscr{G}_c$ inter-laminar fracture energy. These properties can be determined via experimental procedures, see [63,28,64,65] and the references therein.

3. Variational formulation and strong forms

Relying on the considerations given in Section 2, the total energy functional of the solid body $\mathscr{B}$, along with the cracks Γ_i and $\Gamma_{\mathfrak{d}_i}$ at any arbitrary instance $t \in [0, T]$ takes the form:

$$\Pi(\mathbf{u}, \Gamma) \approx \Pi(\mathbf{u}, \mathfrak{d}_i, \mathfrak{d}_c) = \Pi_{int}(\mathbf{u}, \mathfrak{d}_i, \mathfrak{d}_c) + \Pi_{ext}(\mathbf{u}), \tag{29}$$

where the internal and external contribution to the energy functional $\Pi(\mathbf{u}, \mathfrak{d}_i, \mathfrak{d}_c)$ read, respectively:

$$\Pi_{int}(\mathbf{u}, \mathfrak{d}_i, \mathfrak{d}_c) = \int_{\mathscr{B}}\left[(1 - \mathfrak{d}_{FF})^2\hat{\Psi}_{FF}(\boldsymbol{\varepsilon}, \mathbf{A}) + (1 - \mathfrak{d}_{IFF})^2\hat{\Psi}_{IFF}(\boldsymbol{\varepsilon}, \mathbf{A})\right]\mathrm{d}\Omega$$
$$+ \int_{\mathscr{B}} P_{FF}\mathscr{G}_{c,FF}\left[\frac{1}{2l_{FF}}\mathfrak{d}_{FF}^2 + \frac{l_{FF}}{2}|\nabla\mathfrak{d}_{FF}|^2\right]$$
$$+ P_{IFF}\mathscr{G}_{c,IFF}\left[\frac{1}{2l_{IFF}}\mathfrak{d}_{IFF}^2 + \frac{l_{IFF}}{2}|\nabla\mathfrak{d}_{IFF}|^2\right]\mathrm{d}\Omega$$
$$+ \int_{\Gamma_i} \mathfrak{g}^T\mathscr{T}\mathrm{d}\mathscr{S}, \tag{30}$$

$$\Pi_{\text{ext}}(\mathbf{u}) = -\int_{\mathscr{B}} \mathbf{f}_v \mathrm{d}\Omega - \int_{\partial\mathscr{B}_t} \bar{\mathbf{t}} \mathrm{d}\partial\Omega, \tag{31}$$

where $\mathbf{f}_v$ is the deformation-independent volume-specific loads.

In the above expression, Eqn.(30), P_{FF} and P_{IFF} are the activation flags, which are activated when the corresponding pucks failure criterion is met. The approximate solution of the stated problem with MPF-CZ can be obtained as a quadruplet of the solution of the following minimization problem:

$$\left(\mathbf{u}^*, \eth_{FF}^*, \eth_{IFF}^*, \mathfrak{g}^*\right) = \underset{\mathscr{S}}{Argmin} \ \Pi(\mathbf{u}, \eth_{FF}, \eth_{IFF}, \eth_c). \tag{32}$$

where, $\quad \mathscr{S} = \left\{ \eth_{FF}, \eth_{IFF} \geqslant 0 \ \text{for all} \ \mathbf{x} \in \mathscr{B} \setminus \Gamma_i, d_c \geqslant 0 \ \text{for all} \ \mathbf{x} \in \Gamma_i \right\}$

enforcing irreversibility of the evolution parameters. One may also argue that $\mathfrak{g}^*$ should be replaced by the $\eth_c$ in the minimization problem, however, it is easy to see that the minimum value of $\mathfrak{g}^*$ also leads to a minimum value of $\eth_c$ from Eqn. (21).

The quadruplet set $\left(\mathbf{u}^*, \eth_{FF}^*, \eth_{IFF}^*, \mathfrak{g}^*\right)$ in Eqn.(32) is solved by taking a variational form of the total internal energy functional (Gateaux derivative) assuming enough regularity of the terms involved. In the infinitesimal setting, considering the irrevisibility of the damage variables set $\mathscr{S}$ for any admissible test function $(\delta\mathbf{u}, \delta\eth_{FF}, \delta\eth_{IFF}, \delta\mathfrak{g})$ in the appropriate space of distribution, a strong form of the field equations can be reduced to the following:

$$\mathrm{div}\left[(1-\eth_{FF})^2\mathbb{C}_{FF}^e : \boldsymbol{\varepsilon} + (1-\eth_{IFF})\mathbb{C}_{IFF}^e : \boldsymbol{\varepsilon}\right] + \mathbf{f}_v = \mathbf{0} \ \text{in} \ \mathscr{B} \setminus \Gamma_i,$$
$$\text{and} \ \boldsymbol{\sigma} \cdot \mathbf{n} = 0 \ \text{on} \ \partial\mathscr{B}_t, \tag{33}$$

$$2(1-\eth_{FF})P_{FF}\mathscr{H}_{FF}(\mathbf{x},t) = \mathscr{G}_{c,FF}\delta_{\eth_{FF}}\gamma(\eth_{FF}, \nabla_{\mathbf{x}}\eth_{FF}) \ \text{in} \ \mathscr{B} \setminus \Gamma_i$$
$$\text{and} \ \nabla_{\mathbf{x}}\eth_{FF} \cdot \mathbf{n} = 0 \ \text{on} \ \partial\mathscr{B}, \tag{34}$$

$$2(1-\eth_{IFF})P_{IFF}\mathscr{H}_{IFF}(\mathbf{x},t) = \mathscr{G}_{c,IFF}\delta_{\eth_{IFF}}\gamma(\eth_{IFF}, \nabla_{\mathbf{x}}\eth_{IFF}) \ \text{in} \ \mathscr{B} \setminus \Gamma_i$$
$$\text{and} \ \nabla_{\mathbf{x}}\eth_{IFF} \cdot \mathbf{n} = 0 \ \text{on} \ \partial\mathscr{B}, \tag{35}$$

$$\mathrm{div}_{\mathfrak{g}}[\boldsymbol{\sigma}_n(\eth_c) + \tau_n(\eth_c)] = 0 \ \text{in} \ \Gamma_i, \tag{36}$$

wherein the previous expressions $\mathrm{div}_{\mathfrak{g}}[\bullet]$ represents the divergence operator taken with respect to $\mathfrak{g}$. The terms $\mathscr{H}_{FF}$ and $\mathscr{H}_{IFF}$ are the crack driving forces related to fiber and inter-fiber failure, respectively. In accordance with the Pucks failure criteria, the crack driving force of each $j = FF, IFF$ are given by:

$$\mathscr{H}_j(\mathbf{x},t) = \xi_j\left[\left\langle \frac{\underset{\tau\in[0,t]}{\max}\hat{\Psi}_j(\mathbf{x},\tau)}{\hat{\Psi}_{j,init}} - 1 \right\rangle_+\right], \tag{37}$$

where ξ_j is a dimensionless fitting parameter that characterizes the damage activation and post peak behaviours from experimental results. $\hat{\Psi}_{j,init}$ is the effective elastic energy for damage initiation in each of $j = FF, IFF$.

The unilateral stationary condition of the total internal energy functional implies that $\delta\Pi_{int} = 0$ for all $(\delta\mathbf{u}, \delta\eth_{FF}, \delta\eth_{IFF}, \delta\mathfrak{g}) > 0$ and $\delta\Pi_{int} > 0$ for $(\delta\mathbf{u}, \delta\eth_{FF}, \delta\eth_{IFF}, \delta\mathfrak{g}) = 0$ along with the irrivisibility and boundedness of $\eth_{FF}, \eth_{IFF}, \eth_c$ leads to the first-order optimality (KKT) conditions for the quasi-static evolution [39,66]. Γ-convergence of the multi phase-field problem in the absence of the interface can be easily derived following the results obtained in [67].

It is worth noting that the irreversible character of the phase-fields and cohesive zone can be reduced to $\mathscr{S}$, this is fulfilled by the history variable embedded by the history variable Eqn.(37). The boundedness of the phase-field variables $\eth_{FF}, \eth_{IFF} \in [0,1]$ is ensured due to the choice of degradation function $(1-\eth_j)^2$ as in [68]. Also, it is important to note that, we have assumed $\nabla_{\mathbf{x}}\eth_j = 0$ due to the compactness property and $\delta\mathbf{u} = 0$ on $\partial\Omega_t$ and $\delta\eth_j = 0$ on $\partial\Omega$, from the variational form which

are reflected in the choice of approximate spaces of test functions as in Section 4, see [58,59].

4. Finite element implementation

In this section, details of the finite element implementation of the proposed model are outlined. A staggered solution scheme is used to solve the system of coupled Partial Differential Equations (PDEs) using an alternating minimization scheme [69]. Consider the discretization of the domain defined as $\mathscr{B} \to \mathscr{B}^e, \Gamma_i \to \Gamma_i^e$ such that the functions $\mathbf{u}^e \in \mathscr{U}_h, \eth_j^e \in \mathscr{U}_\eth(\eth_j)$ for $j = FF, IFF$ are well defined along with the space of approximate functions:

$$\mathscr{U}_h(u) = \left\{ u \in H^1(\mathscr{B}) | \nabla u \in L^2(\mathscr{B}); u = u_d \ \text{on} \ \partial\mathscr{B}_d \right\}, \tag{38a}$$

$$\mathscr{U}_\eth(\eth_j) = \left\{ \eth_j \in H^1(\mathscr{B}) \bigg| \eth_j(\mathbf{x}) \in [0,1], \dot{\eth}_j \geqslant 0, \forall\mathbf{x} \in \mathscr{B} \right\}. \tag{38b}$$

Similarly, the approximate space for the test functions (distrubutional spaces) for $\delta\mathbf{u}^e \in \mathscr{V}_h, \delta\eth^e \in \mathscr{U}_{\delta\eth}(\eth_j)$ for $j = FF, IFF$ takes the form:

$$\mathscr{V}_h(\delta u) = \left\{ \delta u \in H^1(\mathscr{B}) | \nabla\delta u \in L^2(\mathscr{B}); \delta u = 0 \ \text{on} \ \partial\mathscr{B}_d \right\}, \tag{39a}$$

$$\mathscr{U}_{\delta\eth}(\delta\eth_j) = \left\{ \delta\eth_j \in H^1(\mathscr{B}) \bigg| \delta\eth_j \geqslant 0, \forall\mathbf{x} \in \mathscr{B} \right\}. \tag{39b}$$

At each element level, in the isoparametric space settings, the triplet of field variables $\left\{\mathbf{u}^e, \eth_{FF}^e, \eth_{IFF}^e\right\}$ as well as their variations $\left\{\delta\mathbf{u}^e, \delta\eth_{FF}^e, \delta\eth_{IFF}^e\right\}$ are approximated using linear first order Lagrangian triplet of shape functions $\left\{\mathbf{N}_i^u, \mathbf{N}_i^\eth, \mathbf{N}_i^\eth\right\}$ at i^{th} node of each element satisfying partition of unity is defined as:

$$\mathbf{u}^e = \sum_{i=1}^{\mathbf{N}_{node}} \mathbf{N}_i^u \mathbf{u}_i^e, \qquad \eth_j^e = \sum_{i=1}^{\mathbf{N}_{node}} \mathbf{N}_i^\eth \eth_{j,i}^e, \tag{40}$$

$$\delta\mathbf{u}^e = \sum_{i=1}^{\mathbf{N}_{node}} \mathbf{N}_i^u \delta\mathbf{u}_i^e, \qquad \delta\eth_j^e = \sum_{i=1}^{\mathbf{N}_{node}} \mathbf{N}_i^\eth \delta\eth_{j,i}^e, \quad \text{for each} \ j = FF, IFF. \tag{41}$$

The triplet of spatial derivatives $\left\{\nabla\mathbf{u}^e, \nabla\eth_{FF}^e, \nabla\eth_{IFF}^e\right\}$ are approximated using the gradients of the shape functions $\left\{\mathbf{B}_i^u, \mathbf{B}_i^\eth, \mathbf{B}_i^\eth\right\}$ at i^{th} node of each element takes the form:

$$\boldsymbol{\varepsilon}^e = \sum_{i=1}^{\mathbf{N}_{node}} \mathbf{B}_i^u \mathbf{u}_i^e, \qquad \nabla\eth_j^e = \sum_{i=1}^{\mathbf{N}_{node}} \mathbf{B}_i^\eth \eth_{j,i}^e,$$

$$\delta\boldsymbol{\varepsilon}^e = \sum_{i=1}^{\mathbf{N}_{node}} \mathbf{B}_i^u \delta\mathbf{u}_i^e, \qquad \nabla\delta\eth_j^e = \sum_{i=1}^{\mathbf{N}_{node}} \mathbf{B}_i^\eth \delta\eth_{j,i}^e, \quad \text{for each} \ j = FF, IFF.$$

Complying with the formulation of interface cohesive element, the displacement jump vector $\mathfrak{g}$ is represented in terms of local frames across the interface Γ_i [57]. Hence, the jump $\mathfrak{g}$ and its variation $\delta\mathfrak{g}$ is approximated using the kinematic jump-displacement operator $\mathbf{B}^\mathfrak{g} = \boldsymbol{R}\mathbf{N}^\mathfrak{g}$ as:

$$\mathfrak{g}^e = \mathbf{B}^\mathfrak{g}\boldsymbol{L}\mathbf{u}^e, \qquad \delta\mathfrak{g}^e = \mathbf{B}^\mathfrak{g}\boldsymbol{L}\delta\mathbf{u}^e, \tag{42}$$

where $\boldsymbol{L}$ matrix computes the difference between the displacement of the upper and lower interface points and $\boldsymbol{R}$ is a rotation matrix that converts integration points from global to the local frame, and $\mathbf{N}_\mathfrak{g}$ represents the standard cohesive shape function, see [13].

The discrete elemental residual vectors for the quadruplet $\left\{\mathbf{u}^e, \eth_{FF}^e, \eth_{IFF}^e, \mathfrak{g}^e\right\}$ can be reduced to the following system of equations:

$$\mathbf{R}_e^{\mathbf{u}} = \int_{\mathscr{B}^e}\left[(1-\eth_{FF})^2(\mathbf{B}^u)^T\bar{\boldsymbol{\sigma}}_{FF} + (1-\eth_{IFF})^2(\mathbf{B}^u)^T\bar{\boldsymbol{\sigma}}_{IFF}\right]\mathrm{d}\mathscr{B}$$
$$- \int_{\mathbf{B}^e}(\mathbf{N}^u)^T\mathbf{f}_v\mathrm{d}\mathscr{B} - \int_{\partial\mathbf{B}_u^e}(\mathbf{N}^u)^T\bar{\mathbf{u}}\mathrm{d}\partial\mathscr{B} + \mathbf{R}_e^\mathfrak{g}, \tag{43}$$

$$\mathbf{R}_e^{\eth_{FF}} = \int_{\mathscr{B}^e}\left\{\left[\frac{\mathscr{G}_{c,FF}}{l_{FF}}\eth_{FF} - 2(1-\eth_{FF})P_{FF}\mathscr{H}_{FF}(\mathbf{x},t)\right](\mathbf{N}^\eth)^T + \mathscr{G}_{c,FF}l_{FF}(\mathbf{B}^\eth)^T\nabla\eth_{FF}\right\}\mathrm{d}\mathscr{B}, \tag{44}$$
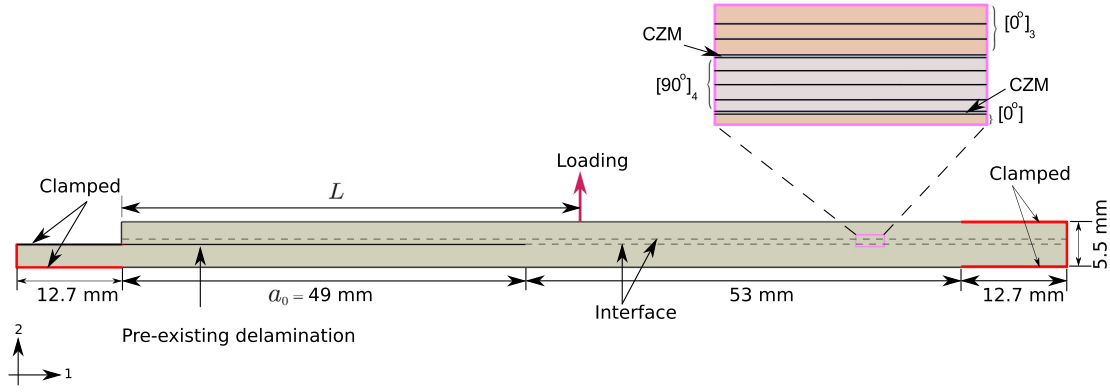
Fig. 4. Schematic representation of the delamination migration model.

$$\mathbf{R}_e^{\mathfrak{d}_{IFF}} = \int_{\mathscr{B}^e} \left\{ \left[\frac{\mathscr{G}_{c,IFF}}{l_{IFF}} \mathfrak{d}_{IFF} - 2(1 - \mathfrak{d}_{IFF}) P_{IFF} \mathscr{H}_{IFF}(\mathbf{x}, t) \right] (\mathbf{N}^{\mathfrak{d}})^T + \mathscr{G}_{c,IFF} l_{IFF} (\mathbf{B}^{\mathfrak{d}})^T \nabla \mathfrak{d}_{IFF} \right\} \mathrm{d}\mathscr{B}. \tag{45}$$

where:

$$\mathbf{R}_e^{\mathfrak{g}} = \int_{\Gamma_i^e} (\mathbf{R}\mathbf{B}^{\mathfrak{g}})^T \mathscr{T}(\mathfrak{g}, \mathfrak{d}_c) \mathrm{d}\mathscr{S}, \tag{46}$$

is the residual vector associated with the cohesive interface. It is clear that the displacement field **u** is strongly coupled with the phase-fields $\mathfrak{d}_{FF}, \mathfrak{d}_{IFF}$ and the displacement jump $\mathfrak{g}$. Whereas, the phase-fields are among themselves and with jump $\mathfrak{g}$ are decoupled which are evident from Eq. (34)–(36) from the assumption that $\Gamma_i \cap \Gamma_{\mathfrak{d}_i} = \varnothing$. Due to the existence of multiple phase-field and interface, the system of equations describing the fracture is non-linear. Hence, an iterative Newton–Raphson solver is used until the convergence in the sense of cauchy sequence $\left[(\mathbf{u}_n^{t+1} - \mathbf{u}_n^t) \right]$ is reached. Here, $\mathbf{u}_n^t$ is the tth iteration at n^{th} step. The corresponding Newton–Raphson iteration to estimate $(n+1)$ time step tales the form:

$$\begin{bmatrix} \mathbf{u} \\ \mathfrak{d}_{FF} \\ \mathfrak{d}_{IFF} \end{bmatrix}_{n+1} = \begin{bmatrix} \mathbf{u} \\ \mathfrak{d}_{FF} \\ \mathfrak{d}_{IFF} \end{bmatrix}_n - \begin{bmatrix} K^{\mathbf{uu}} + K^{\mathfrak{gg}} & 0 & 0 \\ 0 & K^{\mathfrak{d}_{FF}\mathfrak{d}_{FF}} & 0 \\ 0 & 0 & K^{\mathfrak{d}_{IFF}\mathfrak{d}_{IFF}} \end{bmatrix}_{n+1}^{-1} \begin{bmatrix} \mathbf{R}^{\mathbf{u}} \\ \mathbf{R}^{\mathfrak{d}_{FF}} \\ \mathbf{R}^{\mathfrak{d}_{IFF}} \end{bmatrix}_n. \tag{47}$$

where the corresponding element stiffness matrices read:

$$\mathscr{K}_e^{\mathbf{uu}} := \frac{\partial \mathscr{R}_e^{\mathbf{u}}}{\partial \mathbf{u}^e} = \int_{\mathscr{B}^e} (\mathbf{B}^u)^T \mathbb{C}^{ep\mathfrak{d}} \mathbf{B}^u \mathrm{d}\Omega, \tag{48}$$

$$\mathscr{K}_e^{\mathfrak{gg}} := \frac{\partial \mathscr{R}_e^{\mathfrak{g}}}{\partial \mathbf{u}^e} = \int_{\Gamma_i^e} (\mathbf{B}^{\mathfrak{g}})^T \partial_{\mathfrak{g}} \boldsymbol{\tau} \mathbf{B}^{\mathfrak{g}} \mathrm{d}\mathscr{S}, $$

$$\mathscr{K}_e^{\mathfrak{d}_{FF}\mathfrak{d}_{FF}} := \frac{\partial \mathscr{R}_e^{\mathfrak{d}_{FF}}}{\partial \mathfrak{d}_{FF}^e} = \int_{\mathscr{B}^e} \left[\frac{\mathscr{G}_{c,FF}}{l_{FF}} + 2 \mathfrak{P}_{FF} \mathscr{H}_{IFF} \right] (\mathbf{N}^{\mathfrak{d}})^T \mathbf{N}^{\mathfrak{d}} + \mathscr{G}_{c,FF} l_{FF} (\mathbf{B}^{\mathfrak{d}})^T \mathbf{B}^{\mathfrak{d}} \mathrm{d}\Omega, \tag{49}$$

$$\mathscr{K}_e^{\mathfrak{d}_{IFF}\mathfrak{d}_{IFF}} := \frac{\partial \mathscr{R}_e^{\mathfrak{d}_{IFF}}}{\partial \mathfrak{d}_{IFF}^e} = \int_{\mathscr{B}^e} \left[\frac{\mathscr{G}_{c,IFF}}{l_{IFF}} + 2 \mathfrak{P}_{IFF} \mathscr{H}_{IFF} \right] (\mathbf{N}^{\mathfrak{d}})^T \mathbf{N}^{\mathfrak{d}} + \mathscr{G}_{c,IFF} l_{IFF} (\mathbf{B}^{\mathfrak{d}})^T \mathbf{B}^{\mathfrak{d}} \mathrm{d}\Omega. \tag{50}$$

In the Eqn (48), $\mathbb{C}^{ep\mathfrak{d}}$ represents the material consistent tangent estimated using the finite difference method as

$$\mathbb{C}^{ep\mathfrak{d}} = \frac{d\boldsymbol{\sigma}_{ij}}{d\boldsymbol{\varepsilon}_{kl}} \approx \frac{\boldsymbol{\sigma}_{ij}(\hat{\varepsilon}^{kl}) - \boldsymbol{\sigma}_{ij}(\hat{\boldsymbol{\varepsilon}})}{\Delta \varepsilon} \tag{51}$$

with $(\hat{\varepsilon}^{kl}) = \varepsilon + \frac{\Delta \varepsilon}{2} (e_k \otimes e_l + e_l \otimes e_k) = \varepsilon + \Delta \boldsymbol{\varepsilon}^{kl}$. Here e_k and e_l are the kth and l^{th} unit vectors, $\Delta \boldsymbol{\varepsilon}^{kl}$ is the strain perturbation with respect to the

components kl and $\Delta \varepsilon$ is the scalar perturbation parameter. Moreover, σ is estimated from Eqn (17) as $\sigma = \mathbb{C} : \varepsilon$.

The previous non-linear system of equations has been implemented in the finite element software ABAQUS. For this purpose, a user-defined UMAT to define the material behaviour is written for the solution of equilibrium equations associated with the displacement field. Whereas, UEL is utilized to create residual and stiffness matrix for each of the two phase-fields using the material behaviour from UMAT for solving the fracture-associated problem.

5. Representative examples

In this section, modeling application to delamination migration is presented. A comprehensive numerical analysis is presented to validate the model against experimental results. In the sequel, a holistic sensitivity analysis is carried out utilizing the variation of the loading application point, ply angle, and initial pre-crack length to understand their effects on delamination migration.

5.1. Description of the numerical model: general aspects

Fig. 4 depicts the baseline configuration under investigation herein. The corresponding numerical model consists of 44 cross-ply IM7/8552 laminates with the layup sequence.

$[90°_4/0°_3/(90°/0°)_{2s}/0°_3/CL/90°_4/CL/0°/0°/(90°/0°)_{2s}/0°/0°/$ $90°_3/0°/90°]$, where CL refers to a cohesive layer. Each ply has a thickness of 0.125 mm. Compared with the experimental sequence as in [15], a PTFE (Polytetrafluoroethylene) layer is replaced by a cohesive layer and in addition, another cohesive layer is added at the interface between the 90°$_4$ and 0° sequence in order to account for delamination migration.

Analyzing the experimental results reported in [16] it becomes evident that, when shear stresses in the model change sign, migration/

Table 1
IM7/8552: Elastic properties.

E_{11} (GPa)	E_{22} (GPa)	G_{12} (GPa)	ν_{12}	ν_{23}
161.0	11.38	5.17	0.03	0.43

Table 2
IM7/8552: intra-laminar fracture properties and phase-field parameters.

$\mathscr{G}_{c,FF}$ (N/mm)	$\mathscr{G}_{c,IFF}$ (N/mm)	l_{FF} (mm)	l_{IFF} (mm)
81.5	0.2774	0.237	0.07

Table 3
Cohesive layer properties.

| Nominal stress (MPa)	Nominal stress in shear (MPa)	Nominal fracture energy (N/mm)	Fracture energy in shear (N/mm)	Power (BK law)
15	15	0.5	0.65	2.17

kinking occurs, and the crack propagates to the $90°_4$ layers facilitating the inter-fiber failure.

For each of the numerical simulations conducted in the sequel, a 2D analysis is carried with an out-of-plane thickness of 8.37 mm. Since, in order to resolve the gradient of the phase field, the mesh size $\bar{h}$ is restricted to $\bar{h} \approx l/4$. Hence, the domain is discretized by employing 960000 4-node quadrilateral plane stress elements with an average element size of 0.04 mm. Each layer of the cross-ply contains at least four elements across its thickness.

The material properties of IM7/8552 ply are shown in Table 1, which areconsistent with the experimental results in [15]. The fracture energy and length scale parameters for the phase-fields chosen according to the material fracture properties are shown in Table 2. The properties of the cohesive layer following [27] are listed in Table 3.

5.2. Numerical-experimental validation

The global failure response for the specimen under consideration is investigated for the load case $L = a_0 = 49$ mm. The numerical-
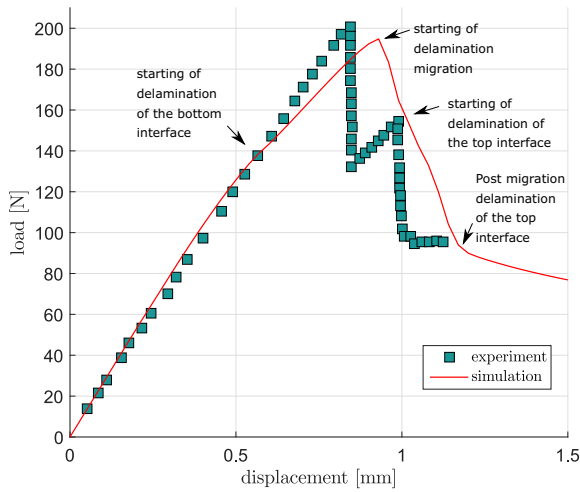
Fig. 5. Numerical-experimental correlation corresponding to the load–displacement curve for $L = a_0 = 49$ mm.
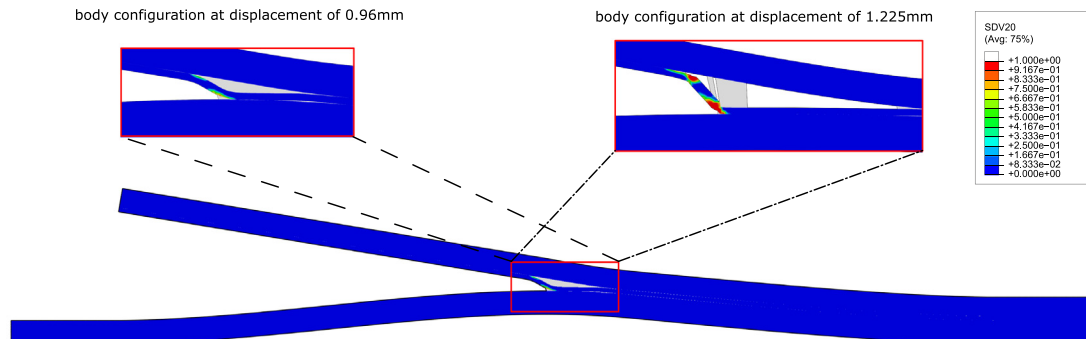
experimental correlation corresponding to the load–displacement curve is given in Fig. 5. As shown in this figure, the failure response can reasonably be divided into three main zones: (i) delamination of the cohesive zone, (ii) kinking followed by migration, and (iii) delamination of the top cohesive zone. Overall, a satisfactory agreement between the numerical and the experimental data can be observed.

As was previously discussed, based on postulations recalled in [15,16] and the corresponding thorough discussion, delamination migration occurs due to a change of sign in the shear stress components. Negative shearing stresses promote delamination growth at the $0°/90°$ interface, and positive shearing stresses promote migration/kinking into $90°$ plies. The kinking happens at multiple sites across the specimen. Due to the diffusive nature of the bulk cracks, the shearing stress change can easily be noticed by the inter-fiber phase-field initiation as depicted in Fig. 6. Notice that, due to the negative sign initially, delamination propagates until a certain point until shearing stresses are positive. Meanwhile, inter-fiber failure is already initiated, but from the opposite direction, i.e., $90°/0°$ interface, but is not nucleated. Whereas, when the shear stresses become positive in the adjacent increments, the migration starts developing, with a crack front now migrating into the $90°/0°$ interface.

For a phenomenology of embodiment, in the cohesive layers, once the failure criterion is met, the cohesive layer starts delaminating. Similarly, when the Puck criterion is violated, the inter-fiber failure phase-field is activated due to shearing stresses in the model. As long as the P_{IFF} is active, the inter-fiber failure phase-field crack $\eth_{IFF}$ grows and migrates into the $90°$ plies until the $90°/0°$ interface. Simultaneously, the top cohesive layer at the $90°/0°$ interface starts to delaminate. When the migration crack front crosses the $90°/0°$ interface, the crack front is again propagating due to the negative shear stress leading to the delamination of the top cohesive layer. Here onward, the residual stresses dominate crack propagation in the model as in Fig. 5. The discrepancies between the experimental and numerical results can be attributed to quasi-static load conditions and smooth initiation and propagation of phase-field approximations. However, a satisfactory agreement between the results can be observed.

5.3. Sensitivity analysis: role of different parameters

This section aims at proving a further understanding with regard to the potential role of different design parameters that can favor delamination-migration events.

Fig. 6. Numerical-experimental correlation corresponding to the load–displacement curve for $L = a_0 = 49$ mm.

5.3.1. Effect of position of loading application

The first aspect under analysis concerns the variation of load application point along the specimen. This parameter in the experimental setting might have a strong influence on the activation of migration phenomena by simply inducing a different local stress field at critical locations. Moreover, from a global standpoint, this can have notable effects on the load–displacement curve as the shear stresses acting on the specimen are significantly different from one another. Keeping $a_0 = 49$ mm, the variation of load L for $L = 0.7a_0, 0.8a_0, 0.9a_0, 1.0a_0, 1.1a_0$ are plotted in Fig. 7.
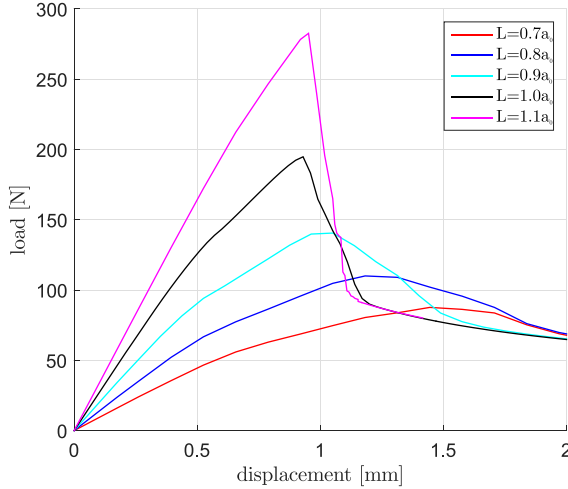
Based on the current results, it can be observed that for $a_0 > L$, all the cases exhibit delamination prior to migration and show a sudden drop in the load-carrying capacity when migration starts, see Fig. 8. Whereas, for $a_0 < L$, the shearing stress sign is favorable for migration at the beginning, and hence there is smooth migration, with delamination spreading over the whole experiment, see Fig. 8 which is consistent with [16]. It is also to notice that after delamination migration is finished, the residual stiffness for delamination converges to a single value for all the load variations.

5.3.2. Effect of the variation of ply angle

The second aspect understudy has an inherent local effect since it focused on investigating the delamination migration at $0°/θ°_4$ interface. For this purpose, the original stacking sequence is replaced by a new layup sequence near the cohesive zones as $0°_3/CL/θ°_4/CL/0°/0°$. The fiber orientation, $θ°$ of $30°, 45°$, and $60°$ is studied along with $90°$, and the results are shown in Fig. 9.

From this graph, it can be seen that the global pre-peak response is almost unaltered by the variation of the local orientation of the adjacent layers to the $0°/θ°_4$ interface. However, this aspect has a notable influence on the post-peak response, delaying the delamination initiation and the subsequent delamination event of the top interface, according to the description given in Fig. 6, but however, the cracking migration is predicted to occur at almost the same loading level (along the post-peak evolution).

5.3.3. Effect of the variation of initial crack length

The last effect under consideration corresponds to the initial crack length. Focusing on very specific cases, we vary initial crack size from $a_0 = 49$ mm to $a_0 = 55$ mm.

The global load–displacement evolution curves for such cases are shown in Fig. 10. According to these data, it can be stated that a simple variation of the initial crack length has a very remarkable role in the
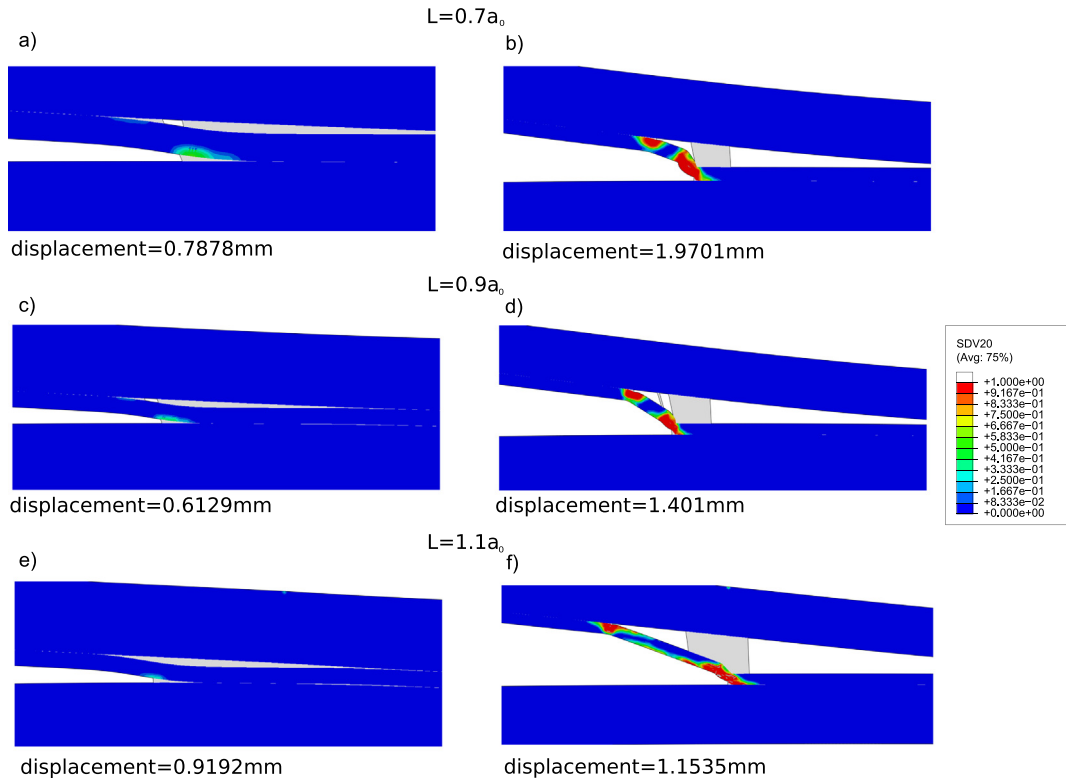

Fig. 7. Variation of load across the specimen for $a_0 = 49$ mm.

Fig. 8. Inter-fiber crack field (SDV20) from 3 cases at $L = 0.7a_0, L = 0.9a_0, L = 1.1a_0$.
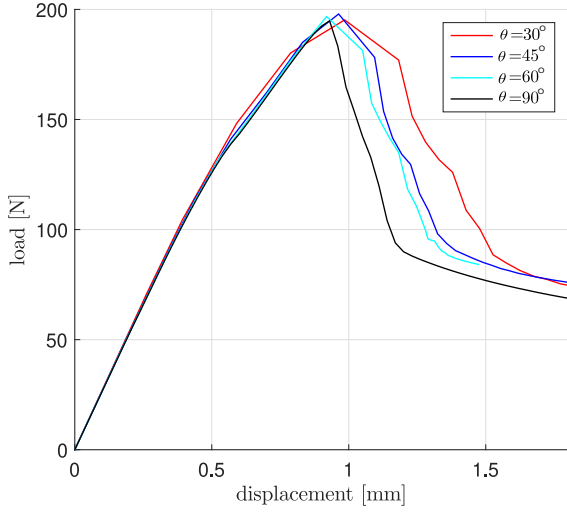
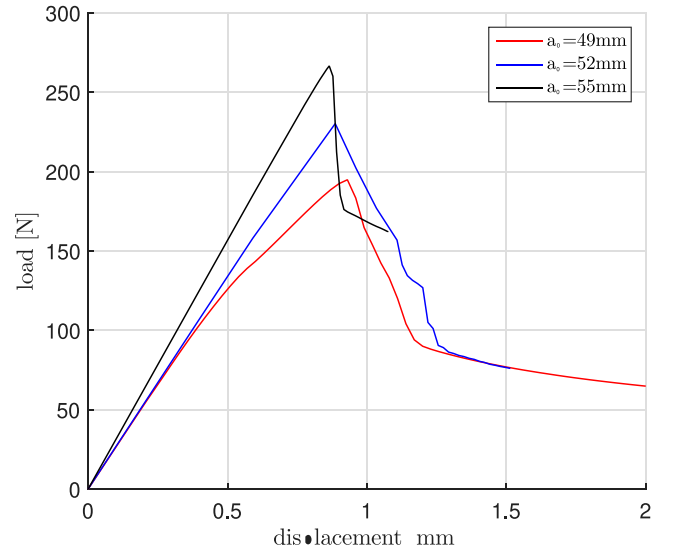**Fig. 9.** Variation of angle across the specimen for $L = a_0 = 49$ mm.

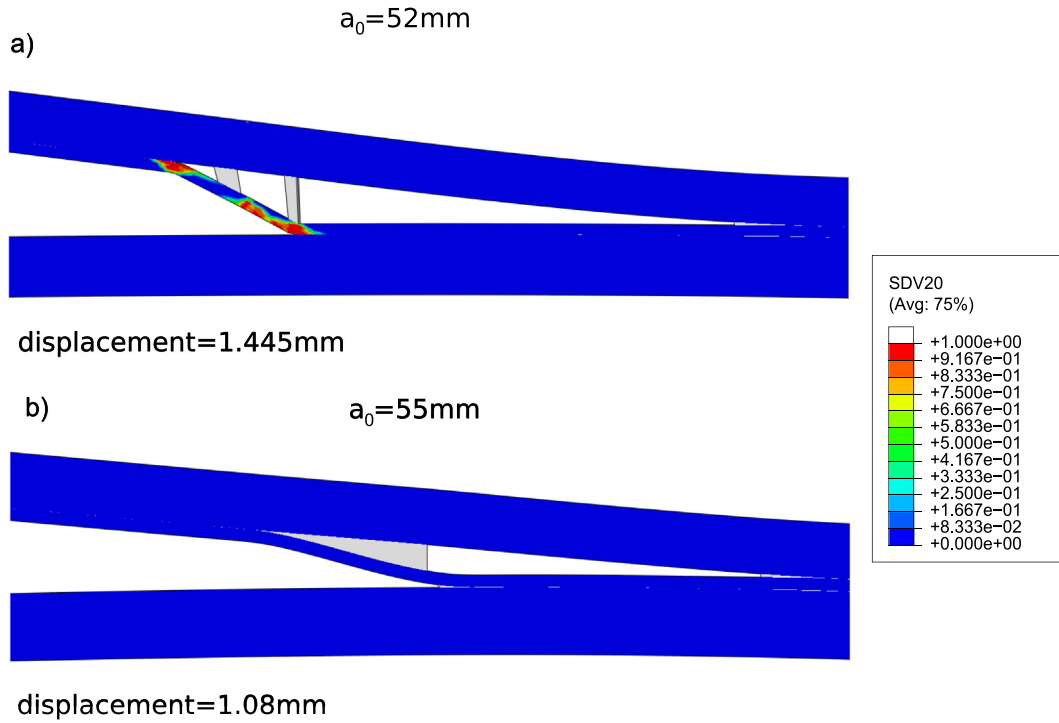**Fig. 10.** Variation of initial crack length across the specimen for $L = a_0$.

Fig. 11. Inter-fiber crack field (SDV20) for initial crack length $a_0 = 52$ mm, $a_0 = 55$ mm with $L = 1.0a_0$.

specimen response. Thus, observing the pre-peak evolution, before any inelastic process commences, the large the initial crack length is set, the higher the maximum load is achieved. Moreover, concerning the post-peak evolution, it is observable that while the shorter initial crack-length case evidence similar evolution with respect to those previously described, i.e., with the occurrence of delamination events and the posterior cracking migration to the adjacent layer, the response of $a_0 = 55$ mm (and $a_0 > 55$ mm) exhibited an entirely different evolution with no evidence of cracking migration, see Fig. 10, and 11 where the matrix-failure maps for both configurations are depicted. These differences in the response are directly associated with the local stress state's discrepancies at the crack tips at the interface and the intermediate layer. This is again in line with previous studies as in [16,15].

6. Conclusion

A consistent multi-phase field-cohesive zone model relying on phenomenological failure criterion has been proposed for matrix-dominated cracking in the presence of interfaces. Due to fiber failure, inter-fiber failure, and interface debonding, the failure mechanism is all accommodated in the model by considering a multi-phase field, each characterized by their failure mechanism with corresponding fracture energy and internal length scale, plus a cohesive zone model.

The computational framework has been carefully derived via multi-field variational formulation with multiple dissipative mechanisms within the spirit of phase-field and cohesive zone models such that thermodynamics consistency is preserved.

The model has been applied to the study of delamination migration in composite materials to illustrate the capabilities of the model. The variation of the design parameters, such as the load application point, the angle between the plies, and the initial crack length, have been presented to assess the model response's sensitivity to such design parameters.

Declaration of Competing Interest

The authors declare that they have no known competing financial interests or personal relationships that could have appeared to influence the work reported in this paper.

Acknowledgements

References

[1] Dean A, Sahraee S, Reinoso J, Rolfes R. Finite deformation model for short fibre reinforced composites: Application to hybrid metal-composite clinching joints. Compos Struct 2016;150:162–71.

[2] Dean A, Reinoso J, Sahraee S, Rolfes R. An invariant-based anisotropic material model for short fiber-reinforced thermoplastics: Coupled thermo-plastic formulation. Compos Part A: Appl Sci Manuf 2016;90:186–99.

[3] Reinoso J, Blázquez A, París F, Cañas J, Meléndez J. Postbuckling behaviour of a pressurized stiffened composite panel – part i: Experimental study. Compos Struct 2012;94(5):1533–43. https://doi.org/10.1016/j.compstruct.2011.12.014. http://www.sciencedirect.com/science/article/pii/S026382231100482X.

[4] Reinoso J, Blázquez A, Estefani A, París F, Cañas J. A composite runout specimen subjected to tension–compression loading conditions: Experimental and global–local finite element analysis. Compos Struct 2013;101:274–89. https://doi.org/10.1016/j.compstruct.2012.12.056. URL: http://www.sciencedirect.com/science/article/pii/S0263822313000883.

[5] Andersons J, König M. Dependence of fracture toughness of composite laminates on interface ply orientations and delamination growth direction. Compos Sci Technol 2004;64(13):2139–52. https://doi.org/10.1016/j.compscitech.2004.03.007. URL: http://www.sciencedirect.com/science/article/pii/S0266353804000752.

[6] Robinson P, Song D. A modified dcb specimen for mode i testing of multidirectional laminates. J Compos Mater 1992;26(11):1554–77. https://doi.org/10.1177/002199839202601101.

[7] Hull D, Shi YB. Damage mechanism characterization in composite damage tolerance investigations. Compos Struct 1993;23(2):99–120. https://doi.org/10.1016/0263-8223(93)90015-I. URL: http://www.sciencedirect.com/science/article/pii/026382239390015I.

[8] Krueger R, Cvitkovich MK, O'Brien TK, Minguet PJ, Testing and analysis of composite skin/stringer debonding under multi-axial loading, Journal of Composite Materials 34 (15) (2000) 1263–1300. arXiv:https://doi.org/10.1177/002199830003401502, doi:10.1177/002199830003401502..

[9] Greenhalgh E, Singh S, Investigation of the failure mechanisms for delamination growth from embedded defects (04 2020)..

[10] Hallett S, Green B, Jiang W, Wisnom M. An experimental and numerical investigation into the damage mechanisms in notched composites. Compos Part A: Appl Sci Manuf 2009;40(5):613–24. https://doi.org/10.1016/j.compositesa.2009.02.021. URL: http://www.sciencedirect.com/science/article/pii/S1359835X09000499.

[11] Reinoso J, Paggi M, Blázquez A. A nonlinear finite thickness cohesive interface element for modeling delamination in fibre-reinforced composite laminates. Compos Part B: Eng 2017;109:116–28.

[12] Turon A, Camanho P, Costa J, Dávila C. A damage model for the simulation of delamination in advanced composites under variable-mode loading. Mech. Mater. 2006;38(11):1072–89. https://doi.org/10.1016/j.mechmat.2005.10.003.

[13] Turon A, Dávila C, Camanho P, Costa J. An engineering solution for mesh size effects in the simulation of delamination using cohesive zone models. Eng. Fract. Mech. 2007;74(10):1665–82. https://doi.org/10.1016/j.engfracmech.2006.08.025.

[14] Turon A, Camanho P, Costa J, Renart J. Accurate simulation of delamination growth under mixed-mode loading using cohesive elements: Definition of interlaminar strengths and elastic stiffness. Compos Struct 2010;92(8):1857–64.

[15] Ratcliffe JG, Czabaj MW, Obrien TK, A test for characterizing delamination migration in carbon/epoxy tape laminates, 2012..

[16] Pernice M, De Carvalho N, Ratcliffe J, Hallett S. Experimental study on delamination migration in composite laminates. Compos Part A: Appl Sci Manuf 2015;73:20–34. https://doi.org/10.1016/j.compositesa.2015.02.018.

[17] Purslow D. Matrix fractography of fibre-reinforced epoxy composites. Composites 1986;17(4):289–303. https://doi.org/10.1016/0010-4361(86)90746-9. URL: http://www.sciencedirect.com/science/article/pii/0010436186907469.

[18] Greenhalgh ES, Rogers C, Robinson P, Fractographic observations on delamination growth and the subsequent migration through the laminate, Compos Sci Technol 69 (14) (2009) 2345–2351, the Sixteenth International Conference on Composite Materials with Regular Papers. doi: 10.1016/j.compscitech.2009.01.034. http://www.sciencedirect.com/science/article/pii/S0266353809000499..

[19] Pernice MF, Ratcliffe J, De Carvalho N, Hallett S, Investigating delamination migration in multidirectional tape laminates, 2014..

[20] He M-Y, Hutchinson JW. Kinking of a Crack Out of an Interface. J Appl Mech 1989;56(2):270–8. https://doi.org/10.1115/1.3176078.

[21] Varandas L, Arteiro A, Catalanotti G, Falzon B. Micromechanical analysis of interlaminar crack propagation between angled plies in mode i tests. Compos Struct 2019;220:827–41. https://doi.org/10.1016/j.compstruct.2019.04.050. URL: http://www.sciencedirect.com/science/article/pii/S0263822318343605.

[22] Canturri C, Greenhalgh ES, Pinho ST, Ankersen J. Delamination growth directionality and the subsequent migration processes – the key to damage tolerant design. Compos Part A: Appl Sci Manuf 2013;54:79–87. https://doi.org/10.1016/j.compositesa.2013.07.004. URL: http://www.sciencedirect.com/science/article/pii/S1359835X13001887.

[23] Pernice M, De Carvalho N, Ratcliffe J, Hallett S. Experimental study on delamination migration in composite laminates. Compos Part A: Appl Sci Manuf 2015;73:20–34. https://doi.org/10.1016/j.compositesa.2015.02.018.

[24] Belytschko T, Gracie R, Ventura G. A review of extended/generalized finite element methods for material modelling. Modell Simul Mater Sci Eng 2009;17:. https://doi.org/10.1088/0965-0393/17/4/043001043001.

[25] Belytschko T, Gracie R, Ventura G. A review of extended/generalized finite element methods for material modeling. Modell Simul Mater Sci Eng 2009;17(4):. https://doi.org/10.1088/0965-0393/17/4/043001043001.

[26] Chen B, Pinho S, Carvalho ND, Baiz P, Tay T, A floating node method for the modelling of discontinuities in composites, Eng Fracture Mech 127 (2014) 104 – 134. doi:https://doi.org/10.1016/j.engfracmech.2014.05.018. http://www.sciencedirect.com/science/article/pii/S0013794414001829.

[27] Li X, Chen J, A highly efficient prediction of delamination migration in laminated composites using the extended cohesive damage model, Compos Struct 160 (10 2016). doi:10.1016/j.compstruct.2016.10.098..

[28] Arteiro A, Catalanotti G, Melro A, Linde P, Camanho P. Micro-mechanical analysis of the effect of ply thickness on the transverse compressive strength of polymer composites. Compos Part A: Appl Sci Manuf 2015;79:127–37. https://doi.org/10.1016/j.compositesa.2015.09.015. URL: http://www.sciencedirect.com/science/article/pii/S1359835X1500336X.

[29] Maimí P, Camanho PP, Mayugo JA, Dávila CG. A continuum damage model for composite laminates: Part I - Constitutive model. Mech Mater 2007;39:897–908.

[30] Reinoso J, Catalanotti G, Blázquez A, Areias P, Camanho P, París F. A consistent anisotropic damage model for laminated fiber-reinforced composites using the 3d-version of the puck failure criterion. Int J Solids Struct 2017:37–53. https://doi.org/10.1016/j.ijsolstr.2017.07.023.

[31] Pijaudier-Cabot G, Bažant ZP. Nonlocal damage theory. J Eng Mech 1987;113 (10):1512–33. https://doi.org/10.1061/(ASCE)0733-9399(1987)113:10(1512).

[32] Bažant ZP, Pijaudier-Cabot G. Nonlocal continuum damage, localization instability and convergence. J Appl Mech 1988;55(2):287–93. https://doi.org/10.1115/1.3173674.

[33] Bažant ZP, Oh BH. Crack band theory for fracture of concrete. Matériaux et Construction 1983;16(3):155–77. https://doi.org/10.1007/BF02486267.

[34] Bažant ZP, Prat PC. Microplane model for brittle-plastic material: I. theory. J Eng Mech 1988;114(10):1672–88. https://doi.org/10.1061/(ASCE)0733-9399(1988)114:10(1672).

[35] Nguyen HT, Pathirage M, Cusatis G, Bažant ZP, Gap Test of Crack-Parallel Stress Effect on Quasibrittle Fracture and Its Consequences, J Appl Mech 87 (7) (may 2020). doi:10.1115/1.4047215..

[36] Nguyen H, Pathirage M, Rezaei M, Issa M, Cusatis G, Bažant ZP. New perspective of fracture mechanics inspired by gap test with crack-parallel compression. Proc Nat Acad Sci 2020;117(25):14015–20. https://doi.org/10.1073/pnas.2005646117. URL: https://www.pnas.org/content/117/25/14015.

[37] Salviato M, Ashari SE, Cusatis G. Spectral stiffness microplane model for damage and fracture of textile composites. Compos Struct 2016;137:170–84. https://doi.org/10.1016/j.compstruct.2015.10.033.

[38] Francfort G, Marigo J-J. Revisiting brittle fracture as an energy minimization problem. J Mech Phys Solids 1998;46(8):1319–42. https://doi.org/10.1016/S0022-5096(98)00034-9.

[39] Bourdin B, Francfort G, Marigo J-J. Numerical experiments in revisited brittle fracture. J Mech Phys Solids 2000;48(4):797–826. https://doi.org/10.1016/S0022-5096(99)00028-9.

[40] Wu J. A unified phase-field theory for the mechanics of damage and quasi-brittle failure. J Mech Phys Solids 2017;103(4):72–99.

[41] Wu J, Nguyen V. A length scale insensitive phase-field damage model for brittle fracture. J Mech Phys Solids 2018;119:20–42.

[42] Dittmann M, Aldakheel F, Schulte J, Wriggers P, Hesch C. Variational phase-field formulation of non-linear ductile fracture. Comput Methods Appl Mech Eng 2018;342:71–94. https://doi.org/10.1016/j.cma.2018.07.029. URL: http://www.sciencedirect.com/science/article/pii/S0045782518303621.

[43] Miehe C, Kienle D, Aldakheel F, Teichtmeister S, Phase field modeling of fracture in porous plasticity: A variational gradient-extended eulerian framework for the macroscopic analysis of ductile failure, Computer Methods Appl Mech Eng 312 (2016) 3–50, phase Field Approaches to Fracture. doi: 10.1016/j.cma.2016.09.028. http://www.sciencedirect.com/science/article/pii/S0045782516305412..

[44] Dean A, Sahraee S, Reinoso J, Rolfes R. A new invariant-based thermo-plastic model for finite deformation analysis of short fibre reinforced composites: Development and numerical aspects. Compos Part B: Eng 2017;125:241–58.

[45] Alessi R, Freddi F. Phase-field modelling of failure in hybrid laminates. Compos Struct 2017;181:9–25. https://doi.org/10.1016/j.compstruct.2017.08.073.

[46] Bleyer J, Alessi R. Phase-field modeling of anisotropic brittle fracture including several damage mechanisms. Comput Methods Appl Mech Eng 2018;336:213–36. https://doi.org/10.1016/j.cma.2018.03.012.

[47] Quintanas-Corominas A, Reinoso J, Casoni E, Turon A, Mayugo J. A phase field approach to simulate intralaminar and translaminar fracture in long fiber composite materials. Compos Struct 2019. https://doi.org/10.1016/j.compstruct.2019.02.007.

[48] Guillén-Hernández T, García IG, Reinoso J, Paggi M. A micromechanical analysis of inter-fiber failure in long reinforced composites based on the phase field approach of fracture combined with the cohesive zone model. Int J Fract 2019. https://doi.org/10.1007/s10704-019-00384-8.

[49] Dean A, Reinoso J, Jha N, Mahdi E, Rolfes R. A phase field approach for ductile fracture of short fibre reinforced composites. Theoret Appl Fract Mech 2020;106:. https://doi.org/10.1016/j.tafmec.2020.102495. URL: http://www.sciencedirect.com/science/article/pii/S0167844219306536102495.

[50] Alkhatib F, Mahdi E, Dean A. Development of composite double-hat energy absorber device subjected to traverser loads. Compos Struct 2020;240:. https://doi.org/10.1016/j.compstruct.2020.112046. URL: https://www.sciencedirect.com/science/article/pii/S0263822319345192112046.

[51] Brod M, Dean A, Scheffler S, Gerendt C, Rolfes R. Numerical modeling and experimental validation of fatigue damage in cross-ply cfrp composites under inhomogeneous stress states. Compos Part B: Eng 2020;200:. https://doi.org/10.1016/j.compositesb.2020.108050. URL: https://www.sciencedirect.com/science/article/pii/S1359836820306624108050.

[52] Martínez-Pañeda E, Golahmar A, Niordson CF. A phase field formulation for hydrogen assisted cracking. Comput Methods Appl Mech Eng 2018;342:742–61. https://doi.org/10.1016/j.cma.2018.07.021. URL: http://www.sciencedirect.com/science/article/pii/S0045782518303529.

[53] Kristensen PK, Martínez-Pañeda E. Phase field fracture modelling using quasi-newton methods and a new adaptive step scheme. Theoret Appl Fract Mech 2020;107:. https://doi.org/10.1016/j.tafmec.2019.102446. URL: http://www.sciencedirect.com/science/article/pii/S0167844219305580102446.

[54] Dean A, Grbic N, Rolfes R, Behrens B-A. Macro-mechanical modeling and experimental validation of anisotropic, pressure- and temperature-dependent behavior of short fiber composites. Compos Struct 2019;211:630–43. https://doi.org/10.1016/j.compstruct.2018.12.045.

[55] Dean A, Asur Vijaya Kumar P, Reinoso J, Gerendt C, Paggi M, Mahdi E, Rolfes R, A multi phase-field fracture model for long fiber reinforced composites based on the puck theory of failure, Compos Struct 251 (2020) 112446. doi:https://doi.org/10.1016/j.compstruct.2020.112446..

[56] Quintanas-Corominas A, Turon A, Reinoso J, Casoni E, Paggi M, Mayugo J. A phase field approach enhanced with a cohesive zone model for modeling delamination induced by matrix cracking. Comput Methods Appl Mech Eng 2020;358:. https://doi.org/10.1016/j.cma.2019.112618. URL: http://www.sciencedirect.com/science/article/pii/S0045782519304943112618.

[57] Paggi M, Reinoso J. Revisiting the problem of a crack impinging on an interface:a modeling framework for the interaction between the phase field approach for brittle fracture and the interface cohesive zone model. Comput Methods Appl Mech Eng 2017;321:145–72. https://doi.org/10.1016/j.cma.2017.04.004. URL: http://www.sciencedirect.com/science/article/pii/S0045782516317066.

[58] Chambolle A. An approximation result for special functions with bounded deformation. Journal de Mathématiques Pures et Appliquées 2004;83 (7):929–54. https://doi.org/10.1016/j.matpur.2004.02.004. URL: http://www.sciencedirect.com/science/article/pii/S0021782404000285.

[59] Ambrosio L, Braides A, Energies in sbv and variational models in fracture mechanics. (1997)..

[60] Tanné E, Li T, Bourdin B, Marigo J, Maurini C. Crack nucleation in variational phase-field models of brittle fracture. J Mech Phys Solids 2018;110:80–99. https://doi.org/10.1016/j.jmps.2017.09.006.

[61] Puck A, Schürmann H. Failure analysis of frp laminates by means of physically based phenomenological models. Compos Sci Technol 2002;62(12):1633–62. https://doi.org/10.1016/S0266-3538(01)00208-1. URL: http://www.sciencedirect.com/science/article/pii/S0266353801002081.

[62] Deuschle HM, Kröplin B-H. Finite element implementation of puck's failure theory for fibre-reinforced composites under three-dimensional stress. J Compos Mater 2012;46(19–20):2485–513. https://doi.org/10.1177/0021998312451480.

[63] Measurement of the compressive crack resistance curve of composites using the size effect law, Composites Part A: Applied Science and Manufacturing 56 (2014) 300 – 307. doi:https://doi.org/10.1016/j.compositesa.2013.10.017. URL http://www.sciencedirect.com/science/article/pii/S1359835X13002923.

[64] Catalanotti G, Xavier J. Measurement of the mode ii intralaminar fracture toughness and r-curve of polymer composites using a modified iosipescu specimen and the size effect law. Eng Fract Mech 2015;138:202–14. https://doi.org/10.1016/j.engfracmech.2015.03.005. URL: http://www.sciencedirect.com/science/article/pii/S0013794415000776.

[65] Camanho P, Dávila C, Pinho S, Iannucci L, Robinson P. Prediction of in situ strengths and matrix cracking in composites under transverse tension and in-plane shear. Compos Part A: Appl Sci Manuf 2006;37:165–76. https://doi.org/10.1016/j.compositesa.2005.04.023.

[66] Borden MJ, Hughes TJ, Landis CM, Verhoosel CV. A higher-order phase-field model for brittle fracture: Formulation and analysis within the isogeometric analysis framework. Comput Methods Appl Mech Eng 2014;273:100–18. https://doi.org/10.1016/j.cma.2014.01.016.

[67] Asur Vijaya Kumar P, Dean A, Reinoso J, Lenarda P, Paggi M, Phase field modeling of fracture in functionally graded materials: Gamma-convergence and mechanical insight on the effect of grading, Thin-Walled Structures 159 (2021) 107234. doi: https://doi.org/10.1016/j.tws.2020.107234..

[68] Miehe C, Hofacker M, Welschinger F. A phase field model for rate-independent crack propagation: Robust algorithmic implementation based on operator splits. Comput Methods Appl Mech Eng 2010;199(45):2765–78. https://doi.org/10.1016/j.cma.2010.04.011.

[69] Bourdin B, Francfort GA, Marigo J-J. The variational approach to fracture. J Elast 2008;91(1):5–148. https://doi.org/10.1007/s10659-007-9107-3.